

# Manipulating molten pool dynamics during metal 3D printing by ultrasound



Cite as: Appl. Phys. Rev. **9**, 021416 (2022); doi: [10.1063/5.0082461](https://doi.org/10.1063/5.0082461)

Submitted: 15 December 2021 · Accepted: 3 May 2022 ·

Published Online: 1 June 2022



View Online



Export Citation



CrossMark

Zhichao Yang,<sup>1</sup> Shuhao Wang,<sup>1,2</sup> Lida Zhu,<sup>1,a)</sup> Jinsheng Ning,<sup>1</sup> Bo Xin,<sup>1</sup> Yichao Dun,<sup>1</sup> and Wentao Yan<sup>2,a)</sup>

## AFFILIATIONS

<sup>1</sup>School of Mechanical Engineering and Automation, Northeastern University, Shenyang 110819, China

<sup>2</sup>Department of Mechanical Engineering, National University of Singapore, 117575 Singapore

<sup>a)</sup>Authors to whom correspondence should be addressed: [neulidazhu@163.com](mailto:neulidazhu@163.com) and [mpeyanw@nus.edu.sg](mailto:mpeyanw@nus.edu.sg)

## ABSTRACT

Ultrasound-assisted direct energy deposition (UADED) attracts increasing attention due to its capability to tailor the grain structure. However, the involved molten pool dynamics, particularly the complex interaction of ultrasound-flow-solidification, remain unclear to date, which hinders quantitative prediction and regulation of the microstructures and mechanical properties of UADED components. Here, *in situ* high-speed imaging and high-fidelity multi-physics modeling are leveraged to investigate flow characteristics and liquid-to-solid transformation in UADED for Inconel 718. The inertial force activated by ultrasound is revealed to drive the molten pool to flow forward and backward along the vibration direction, resulting in poor surface quality. A hybrid deposition strategy is developed to minimize ultrasound-induced defects and produce superior microstructure with alternating coarse- and fine-grains. Such a layered microstructure results in 28% and 15% improvement in the yield strength and ultimate tensile strength compared to the counterpart by additive manufacturing without ultrasound. This work provides unprecedented understanding into the molten pool dynamics in the UADED process as well as valuable guidance to manipulate molten pool flow.

Published under an exclusive license by AIP Publishing. <https://doi.org/10.1063/5.0082461>

## I. INTRODUCTION

Directed energy deposition (DED), an important subset of metal additive manufacturing (AM), endows the manufacturing industry with its flexibility on repairing and fast near-net-shape forming.<sup>1–3</sup> The fast solidification and large temperature gradient during DED could lead to improvement in the overall mechanical performance because of hierarchical structures.<sup>4,5</sup> However, these AM features also induce cross-layer columnar grains and multiple internal defects, which can downgrade the mechanical properties.<sup>6</sup> These Achilles heels are hindering DED development.<sup>7,8</sup> Refining microstructures of the as-built parts has proven to be useful for mitigating the property anisotropy and improving their mechanical performance.<sup>9,10</sup> Some studies achieve this goal via applying special scanning strategies or laser beam intensity modulations during the metal printing process.<sup>11–13</sup> However, this kind of method is difficult to exert sufficient control on producing 100% equiaxed grains, because the extremely high temperature gradient in metal AM promotes the epitaxial growth of columnar grains.<sup>10,14</sup> The more extensively utilized method, named inoculation treatment, is introducing dispersed nanoparticles such as TiC, SiC, TiB<sub>2</sub>, LaB<sub>6</sub>, and TiCN, into the molten pool to promote the nucleation of the new grains and, thus, refine the microstructures.<sup>10,15–17</sup>

Nevertheless, the major shortcomings are that the foreign particles inevitably contaminate the alloy and may agglomerate together to form clusters due to the high viscosity.<sup>17,18</sup> Thus, a flexible and universal modification method without introducing foreign particles is required to tailor the microstructures and enhance mechanical properties.<sup>18–20</sup>

High-intensity ultrasound has often been used for such purposes in metal forming, including welding,<sup>21,22</sup> casting,<sup>23,24</sup> and AM.<sup>25–27</sup> Particularly, the full transition from columnar grains to fine equiaxed grains in AM has been achieved by employing ultrasound recently.<sup>18</sup> The results demonstrate great improvements in both yield strength and tensile strength compared with the counterpart by AM without ultrasound. Most of the studies report that it is the ultrasound induced cavitation, which leads to the transition from coarse to fine grains. Nowadays, the common view of the action mechanism is that the behaviors of the cavitation bubble or cloud mechanically break the dendrites into pieces, which can act as the heterogeneous nucleation catalysts during crystallization.<sup>28,29</sup> In addition, the cavitation bubbles emit high temperature and high-pressure shock waves after bursting,<sup>30</sup> which stir the melted materials to activate the nuclei in the molten pool during the solidification.<sup>31,32</sup>

It should be noted that melt flow characteristics also play a significant role in the solidification process and the microstructures. However, the comprehensive insight into the DED process with ultrasound has not been reported to date. Research studies mainly focuses on the laser-material interaction in the laser-based metal AM without ultrasound, which directly affects the heat and mass transfer.<sup>33–35</sup> Metal droplets, molten pool and unstable metal vapor are the most remarkable results of the interaction in metal AM.<sup>36,37</sup> These instantaneous phenomena in the molten pool can be captured and studied by *in situ* high-speed imaging method and high-fidelity multi-physics simulations.<sup>38,39</sup> Overall, the melt flow in the molten pool presents different patterns, including outward centrifugal flow, inward centripetal flow, and depression, under the effects of two major driving forces, namely, Marangoni force and recoil pressure.<sup>39–42</sup> Nevertheless, ultrasound can introduce additional force into the molten pool during ultrasound-assisted direct energy deposition (UADED), which may compete for the dominate role with the aforementioned driving forces, and then change the flow mode of the melt. Therefore, an in-depth understanding about flow characteristics and liquid to solid transformation during UADED is essential to guide manufacturing process optimization and part properties improvement.

To thoroughly understand the complex molten pool behavior that occurs in a very short time ( $10^{-6}$ – $10^{-3}$  s),<sup>39,43</sup> we leverage high-fidelity simulations and *in situ* monitoring experiments with a high-speed camera to probe the molten pool morphology and uncover the inside flow characteristic. Inconel 718 with high temperature strength, good oxidation and corrosion resistance, good fatigue performance, and fracture toughness is used as the model material in this study. The effect of the ultrasound on the molten pool dynamics is then elucidated at a microsecond temporal scale (4  $\mu$ s). By quantitatively evaluating the dimensions of transverse cross section of the solidified tracks, the relationships between the parameters and the track geometries are established and the formation mechanism of the surface imperfections of the UADED fabricated tracks is revealed. A hybrid deposition method is proposed to obtain high-quality parts with an alternating coarse- and fine- microstructure, leading to considerable improvement in both the yield strength and ultimate tensile strength, respectively.

## II. MATERIALS AND METHODS

### A. Sample preparation

To explore the evolution of molten pool dynamics during UADED, an experiment system was built, which included a laser deposition processing center SVW80C-3D (made by Dalian Sunlight Technology Co. Ltd., China, and consisting of a YSL-2000 fiber laser source with a spot diameter of 2.4 mm, powder feeder, and protective gas device), ultrasonic vibration auxiliary devices (ultrasonic generator, transducer, and horn), and a high-speed camera that can collect data in real time and monitor changes in the molten pool and powder flow (Fig. S1). The shielding gas used in this study is nitrogen and the total flow rate is 3.50 l/min together with the carrier gas. For the ultrasonic vibration system, the substrate connected coaxially with the transducer through the horn, that is, the vibration direction remained parallel to the scanning direction during the deposition process. A No. 45 steel plate was selected as the substrate (its size was  $100 \times 50 \times 50$  mm<sup>3</sup>), and Inconel 718 with high temperature strength, good oxidation and corrosion resistance, good fatigue performance, and fracture toughness<sup>44,45</sup> is used as the powder material. The size distribution of the

powders and the morphology were obtained by using the scanning electron microscope (SEM) [Fig. S1(d)]. The diameter of the powder was roughly normal, ranging from 20 to 80  $\mu$ m. The powder compositions are listed in Table S1. The ultrasonic vibration auxiliary devices converted a low-frequency current signal of 50 Hz into a high-frequency current signal (19.8 kHz)<sup>46</sup> and further converted into a high-frequency vibration with an amplitude of 10  $\mu$ m through a transducer made of piezoelectric ceramics, thereby realizing UADED. A laser displacement sensor was used to monitor the actual vibration state of the substrate during the deposition process [Fig. S1(c)]. The *in situ* monitoring system was employed to capture the deposition details in DED and UADED. A high-speed camera 5KF20 (made by FuHuang AgileDevice, Hefei, China) was used [Figs. S1(a) and S1(b)]. The maximum frame rate and corresponding exposure time are 8000 fps and 1  $\mu$ s. Before recording the video, the camera software was calibrated for distance measurement and a number of pixels with the given length in the captured video was specified. The high-speed camera was  $\sim$ 15 mm away from the substrate and perpendicular to the scanning direction. The angle between the central axis of the camera and substrate was 50°. The flow characteristics of the melted materials were recorded with a frame rate of 5000 Hz. A laser illumination source, together with a narrow bandwidth filter that matches the wavelength of the illumination laser (808 nm), was used to block noise and improve the quality of the images.

### B. Microstructure characterization and tensile testing

The main phases formed are  $\gamma$ -Ni, Fe and  $\gamma'$ -Ni<sub>3</sub>(Al, Ti) by x-ray diffraction tests [Fig. S1(e)]. The strongest diffraction peak appears at approximately 43°, which corresponds to the (111) crystal plane. Crystal planes such as (200), (220), (311), and (222) also produced diffraction peaks.

The samples with dimensions of  $5 \times 5 \times 2$  mm<sup>3</sup> (length  $\times$  width  $\times$  height) cubes were used for microstructural characterizations. Before the analysis of microstructure characteristics, the metallographic cross sections of the specimens were obtained through a series of post-processing, including wire electrical discharge machining (EDM), grinding, mechanical polishing, ultrasonic cleaning, and corroding (25 ml HCl + 25 ml C<sub>2</sub>H<sub>6</sub>O + 2 g CuCl<sub>2</sub>).<sup>47</sup> The dendrite morphology and the precipitated phase were observed by A MIRA3 TESCAN scanning electron microscope (SEM). Additionally, an argon ion beam system (Ilion II System, Model 697) was used to polish the samples (ion beam energy of 5 keV and specimen stage rotation of 3 rpm for 1 h) for electron backscatter diffraction (EBSD) analysis. EBSD analysis (accelerating voltage of 25 kV, probe current of 18 nA, step size of 1.0  $\mu$ m) was conducted using an SEM (Zeiss, Crossbeam 550) equipped with an Oxford EBSD detector. The texture data and orientation information were obtained by the Channel 5 Analysis™ software package.<sup>48</sup>

The as-deposited AM Inconel 718 parts were cut into flat tensile specimens transverse to the build direction with a gauge length of 13 mm, width of 3 mm, and thickness of 1 mm. Tensile testing with an initial strain rate of  $3.85 \times 10^{-4}$  s<sup>-1</sup> was performed on three specimens per condition using a universal testing machine (made by Sinotest Equipment Co., Ltd. DNS 10). The critical experimental parameters are as follows:  $P = 800$  W (Laser power),  $S = 600$  mm/min (Scanning speed), and  $F = 18.62$  g/min (powder feeding rate).

### C. Multi-physics modeling

The molten pool dynamics and solidified cladding track morphology were simulated by multi-physics thermal-fluid flow models. These multi-physics models were customized on the commercial software FLOW-3D. The molten fluid flow was assumed to be incompressible, laminar, and Newtonian, and governed by the conservations of mass, momentum, and energy. Details regarding the governing equations for DED cases can be found in our previous work.<sup>49–52</sup> For the UADED cases, the coordinate system is fixed on the substrate, which is a non-inertial reference system. The ultrasound induced inertial force is incorporated into the momentum conservation equation, which is given in the following equation:

$$\frac{\partial}{\partial t}(\rho \mathbf{v}) + (\mathbf{v} \cdot \nabla) \rho \mathbf{v} = \nabla \cdot (\mu \nabla \mathbf{v}) - \nabla p + \mathbf{f}_B + \mathbf{S}_D + \mathbf{S}_u, \quad (1)$$

where  $\rho$  and  $\mu$  represent the density and viscosity, respectively.  $\mathbf{v}$  denotes the flow velocity,  $p$  is the pressure,  $\mathbf{f}_B$  denotes the buoyant force calculated based on the Boussinseuq approximation,  $\mathbf{S}_D$  is the Darcy force, and  $\mathbf{S}_u$  denotes the inertial force induced by the ultrasound, as given in the following equation:

$$\mathbf{S}_u = -\rho f^2 A \sin(\theta), \quad (2)$$

where  $f$  is the angular frequency of the ultrasound, and  $A$  denotes the oscillation amplitude. The frequency and amplitude of the oscillation are assumed to remain constant in the simulation. Molten pool surfaces were tracked using the volume of fluid method,<sup>53</sup> and the Marangoni force, surface tension, and recoil pressure were treated as the boundary conditions. In addition, the relative vibration was implemented into the laser heat source model of UADED cases, as given in the following equation:

$$A_{\text{oscillation}} = -A \sin(\theta), \quad (3)$$

where  $A_{\text{oscillation}}$  denotes the displacement of the laser relative to the substrate along the scanning direction. For the normal DED case, the laser power absorptivity is 0.22, while that for UADED is higher, since laser rays are reflected multiple times on the depressed molten pool surface. In this regard, the average laser power absorptivity for the UADED case is 0.35 in this study, which is calculated using the ray-tracing method.<sup>54,55</sup> The powder source structure presents a quad nozzle arrangement and the powder stream injection angle is approximately 60°, which follows the experimental measurements [Figs. S2(b) and S2(c)]. The motions of the spherical powder particles were traced with a Lagrangian particle model, efficiently and accurately.<sup>56</sup> The individual powder particles can exchange mass, thermal energy, and kinetic energy with the molten pool when they collide with the host fluid. The material properties for Inconel 718 used in simulations are listed in Table S2 and S3.<sup>57,58</sup> The simulation domain is 62 × 34 × 19 mm<sup>3</sup>, where the minimum mesh size was 25 μm (for the molten pool region). The simulation results were recorded every 4 μs to ensure that all thermal behaviors of the molten pool can be well recognized.

### D. Cavitation judgment

The main limitation of this study is that the cavitation phenomenon cannot be directly proved to exist in UADED. We did not capture clear images of the cavitation bubbles in the experiments, nor

reproduce cavitation phenomenon in the simulation cases. Instead, we adopted a calculation method proposed in Ref. 18 to judge whether the cavitation would happen. The ultrasound intensity is given in the following equation:

$$I = \frac{1}{2} \rho c (2\pi f A)^2, \quad (4)$$

where  $I$  represents the ultrasonic intensity,  $\rho$  is the density of Inconel 718 in the liquid state, and  $c$  denotes the sound velocity in the liquid. The calculated ultrasonic intensity is >2 × 10<sup>7</sup> W m<sup>-2</sup> at  $A = 10 \mu\text{m}$ , where  $c = 4047 \text{ m s}^{-1}$  (Ref. 59) for molten Ni, which is much larger than the cavitation threshold ( $\sim 10^6 \text{ W m}^{-2}$ ) in the Ref. 32. That is, the employed ultrasound has great potential to produce cavitation bubbles in the molten pool.

## III. RESULTS AND DISCUSSION

### A. Flow characteristics

The flow and solidification of molten pool are closely related to the manufacturing quality. Critical phenomena, including the molten pool morphologies and powder state, are clearly captured through *in situ* high-speed imaging to depict discrepancy between DED and UADED [Figs. 1(b) and 1(d), Multimedia view]. Unlike the molten pool of DED with relatively convex, stable surface, the molten pool of UADED shows depression with fish-scale ripples additionally accompanied by a narrow but long regime at the rear-end [Figs. 1(b) and 1(d),  $t = 0$  to  $t = 7.20 \text{ ms}$ , Figs. S3(a)–S3(c)], hereafter referred to as the tail zone. Besides, with respect to UADED, a few unmelted powders can be observed at the tail zone, where the melt is shallower and cooler than that at the center [Fig. S3(d)]. The residence time of these powders is  $\sim 13.66 \text{ ms}$ . We use multi-physics computational fluid dynamics (CFD) models to perfectly reproduce the respective manufacturing process of DED and UADED. Simulation results deliver great agreement with those experimental phenomena, including molten pool morphologies, depression, and uniform fish-scale ripples on the molten pool surface during UADED [Figs. 1(a) and 1(c), Multimedia view]. The presented streamlines [Figs. 1(e)–1(h) and S4(a) and S4(b)] clearly indicate that the flow modes are different during DED and UADED. The flow mode of DED depicts a typical centrifugal Marangoni flow, where melt flows from center (laser centrum location) toward the edge on the molten pool surface, and then back beneath the surface. Whereas there is no significant Marangoni convection during UADED; the melted materials periodically flow forward and backward, along the vibration direction. Furthermore, fluid velocity of UADED is larger than that of DED.

To further our understanding of the unique molten pool dynamics during UADED, we investigate the specific flow patterns in different cross sections of the molten pool [Figs. 2(a) and 2(b-B1)–2(b-B4), Multimedia view]. Figure 2(b-B4) shows the central longitudinal cross section of the molten pool: the representative flow patterns uncover that the ultrasound-induced inertial force plays a dominant role in the molten pool dynamics. The inertial force drives the melted materials to flow forward and backward along the scanning direction, which significantly enlarges the molten pool length. More profoundly, the bidirectional flow mode also gives rise to the depressed molten pool surface, and reduces convection inside the molten pool. For normal DED dominated by Marangoni force, the flow mode in the molten

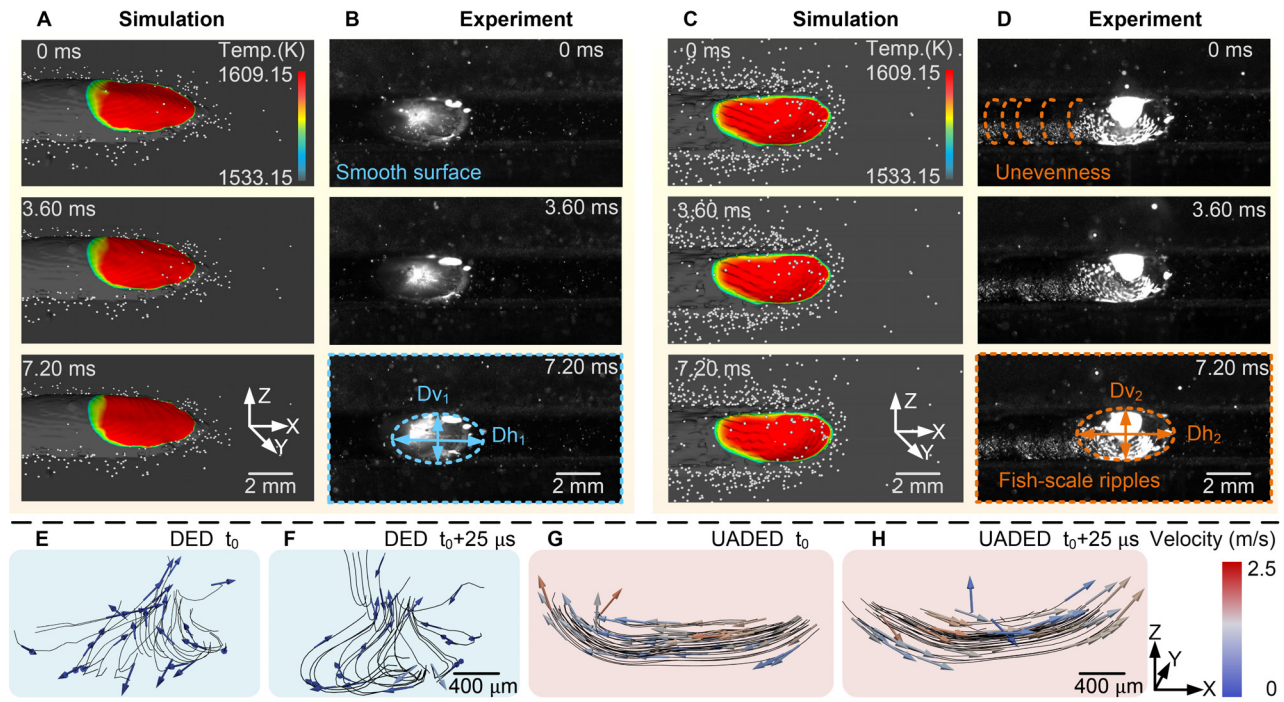


**FIG. 1.** Molten pool evolution under the ultrasound effect. (a) and (c) Simulation results (molten pool morphology, temperature field, and flow field) of the dynamic molten pool without and with ultrasound, respectively. (b) and (d) A series of optical images with the time interval of 3.6 ms display the instantaneous molten pool morphology for DED and UADED, respectively, in which  $Dv_1$  and  $Dh_1$  mark out the dynamic molten pool width and length during DED, and  $Dv_2$  and  $Dh_2$  are the dynamic molten pool width and length during UADED. (e) and (f) and (g) and (h) Flow field streamlines in the molten pool during DED and UADED, respectively. Vector arrows represent the fluid velocity directions, and color bar denotes the magnitude of fluid velocity. Manufacturing parameters are as follows:  $P = 800$  W (laser power),  $S = 360$  mm/min (scanning speed), and  $F = 4.04$  g/min (powder feeding rate). Multimedia views: <https://doi.org/10.1063/5.0082461.1>; <https://doi.org/10.1063/5.0082461.2>; <https://doi.org/10.1063/5.0082461.3>; <https://doi.org/10.1063/5.0082461.4>

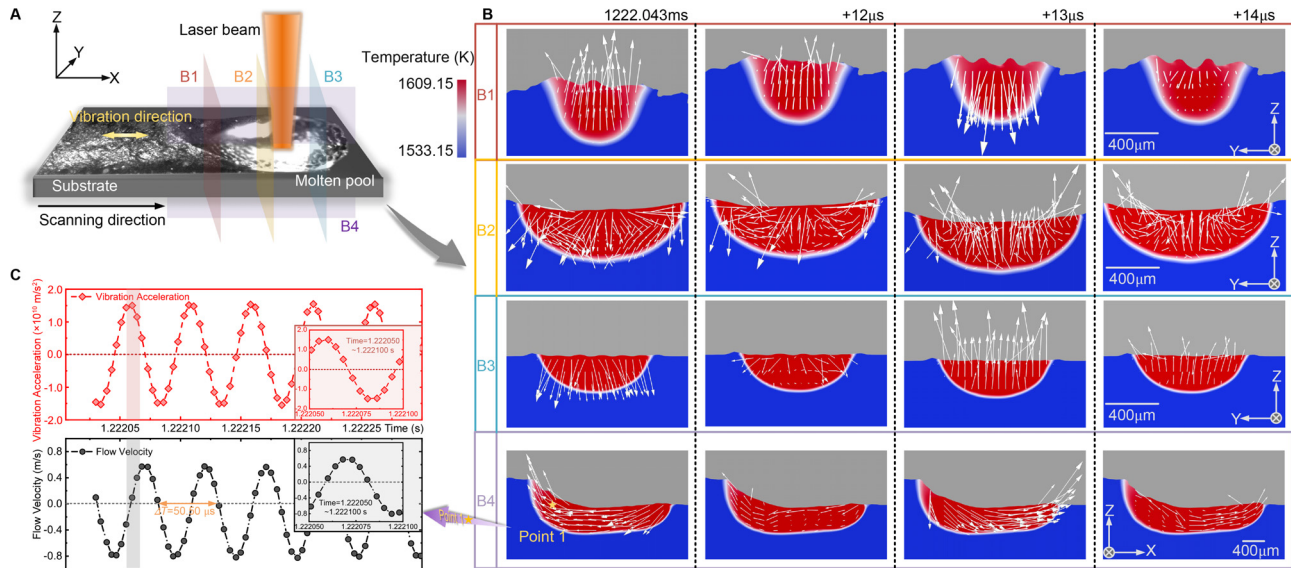


**FIG. 2.** Flow characteristics of the molten pool in UADED. (a) and (b) Flow characteristics at different sections along the longitudinal direction (rear cross section B1, middle cross section B2, front cross section B3) and the transverse direction (B4), where the arrows represent the melt velocity projection on the plane, including the magnitude and direction. (c) The flow velocity at point 1 in cross section B4 and vibration acceleration. The inset in (c) shows the flow velocity and vibration acceleration in one cycle ( $\Delta T = 50.50 \mu\text{s}$ ). Multimedia views: <https://doi.org/10.1063/5.0082461.5>; <https://doi.org/10.1063/5.0082461.6>; <https://doi.org/10.1063/5.0082461.7>; <https://doi.org/10.1063/5.0082461.8>

pool is always centrifugal convection flow or centripetal convection flow, which results in the convex molten pool surface.

However, the magnitude of the inertial force is much larger than those of other driving forces, inducing barely any convection parallel to the X-Z plane during UADED. All the melted materials fast oscillate in the valley between the substrate and the solidified track, thus the centrifugation causes the depression on the molten pool surface. [Figure 2\(c\)](#) shows the local x-velocity at probe point 1. The velocity presents a sinusoidal variation and the period is  $\sim 50.50 \mu\text{s}$ , which is identical to the period of the ultrasound.

A dominant mechanism for the formation of the uniform fish-scale ripples is that the ultrasound-induced inertial force drives the molten pool fluctuation. The molten pool surface is tilted at certain angles to the vibration direction because of the depression. When the inertial force acts on the surface, it makes the surface reciprocate. The rapidly alternating peaks and troughs then turn a uniform fish-scale ripple pattern on the molten pool surface. The transverse cross sections at the rear-end, middle and front-end of the molten pool in UADED show the periodic upward and downward flow patterns. The velocity fields on these transverse cross sections shed light into a secondary formation mechanism of the uniform fish-scale ripples on the molten pool surface. Specifically, the velocity vectors distribute uniformly inside the molten pool, but cluster near the surface, and thus form some uniform peaks and troughs [[Fig. 2\(b-B1\)](#)]. We attribute this phenomenon to the surface tension. As shown in [Fig. S5\(a\)](#), the distribution of the temperature indicates that several low temperature regions exist on the molten pool surface. Surface tension gradient drives the melted materials to the low temperature regions. The unevenness at the rear-end presents most serious among the cross sections [[Figs. 2\(b-B1\)–2\(b-B3\)](#)]. This is because the laser is near the middle and front end of the molten pool, providing more energy and reduce the amounts of the low temperature regions [[Figs. S5\(b\) and S5\(c\)](#)]. Not only the periodic upward and downward flow, but also the convection arises in the middle transversal cross section. During UADED, the rapid relative motion between laser and substrate increases the area of the high-temperature region at the molten pool center. Marangoni force drives the melt from center to the edge, enlarging the molten pool width and forming a relatively smooth surface in the middle cross section.

The multi-physics model is extended to investigate the molten pool dynamics under the effect of low frequency vibration (3150 Hz). Similarly, the unique depression and fish-scale ripples are also observed on the molten pool surface. A major difference is that the tail zone in the low frequency case is not obvious, thus the molten pool shape is rounder than that of the high frequency UADED case [[Figs. S6\(a\)–S6\(e\)](#)].

As shown in [Fig. 3](#), the bright debris is observed floating on the molten pool surface, which is possibly related to the gas bubbles, high melting point metal oxides,<sup>43,60</sup> or unmelted powder particles.<sup>61</sup> Spatters are observed to be released from the debris during both DED and UADED. The whole process of spattering droplets escaping from the molten pool is well depicted by [Figs. 3\(c\) and 3\(d\)](#). Obviously, the spatters are more frequent in UADED [[Figs. 3\(a\) and 3\(b\)](#)]. We extract the information of these spatters from a series of sequent images [such as [Figs. 3\(c\)–3\(f\)](#)] and quantify their initial velocities and sizes when they are emitted from the molten pool. Interestingly, the spatters in UADED behave very differently with the counterparts in DED, particularly in the size and velocity. The spatters during

UADED distribute more widely in diameter, and have a larger average diameter than those in DED (UADED 103.31 vs DED 58.1  $\mu\text{m}$ ), while spatters during DED distribute more widely in velocity, and have a larger average velocity (DED 1.04 vs UADED 0.62 m/s). This indicates that the major formation mechanisms are different for spatters in UADED and DED. A criterion to evaluate whether the micro-droplets can detach from the molten pool is given in the following equation:<sup>62</sup>

$$\rho_l v^2 > \frac{2\sigma}{R}, \quad (5)$$

where  $\rho_l$  represents the melt density,  $v$  denotes the melt velocity,  $\sigma$  is the surface tension, and  $R$  is the local curvature radius of the melt surface. Therefore, when the melt velocity is higher than a threshold, spatters generate. In this study, we calculate the velocity thresholds for both UADED and DED cases, using the material density and surface tension at liquidus temperature, and the average radii of the spatters during UADED and DED as the curvature radius. The calculated velocity thresholds for UADED and DED are 3.1 and 4.14 m/s, respectively. It should be noted that the curvature radius is usually larger than the spatter radius, so the velocity thresholds are overestimated to some extent. As illustrated by the simulation, the melt surface velocity in DED is smaller than 1 m/s [[Fig. S4\(b\)](#)], which means that the detaching process rarely happens. In contrast, the melt surface velocity can reach 2.5 m/s during UADED, which is close to the velocity threshold. In addition, the surface peaks induced by the inertial force can promote the micro-droplets separating from the molten pool. Thus, the dominant formation mechanism for spatters during UADED is micro-droplets detaching from molten pool [[Fig. 3\(d\)](#)]. Dissimilarly, most of the spatters during DED are associated with localized overheating, since they are observed accompanying with the metal vapor [[Fig. 3\(c\)](#)].<sup>63</sup> Consequently, the spatters during DED are small and fast.

Here, the dynamic molten pool length and width are considered as the intuitive indices to quantitatively evaluate the molten pool morphologies. According to the statistical results, they are positively correlated with the laser power while negatively with the scanning speed. However, their dependence on the powder feed rate is not remarkable, suggesting that the laser attenuation by powder particles is not significant. Furthermore, both the molten pool length and width during UADED are larger than those during DED with the same parameter sets [[Fig. 4\(d\)](#)]. This is because laser absorptivity is larger during UADED. For solidified tracks, we mainly compare the values of track depth and track width between DED and UADED, since the track height of UADED is inconsistent [[Fig. 4\(a\)](#)]. In the present study, most of the UADED cases are in the transition mode (between conduction and keyhole modes), while the DED cases with same parameter sets are in the conduction mode.  $A_1$  and  $A_2$  depict two representative cross section morphologies of the UADED fabricated tracks, where depressions arise at both sides of the tracks. This phenomenon is caused by the aforementioned narrow tail zone and the depression on the molten pool surface during UADED. Almost all the DED cases are below the black dot line, which indicates that the solidified tracks in DED are wider but shallower than those in UADED [[Fig. 4\(b\)](#)]. Because of the insufficient dilution during DED (see  $B_1$  and  $B_2$ ), the solidification front at either side of molten pool is above the substrate [[Fig. 1\(b\)](#)], which results in the actual solidified width to be larger than the molten pool width. This explains why the DED molten pools are narrower, but the solidified tracks are wider than those

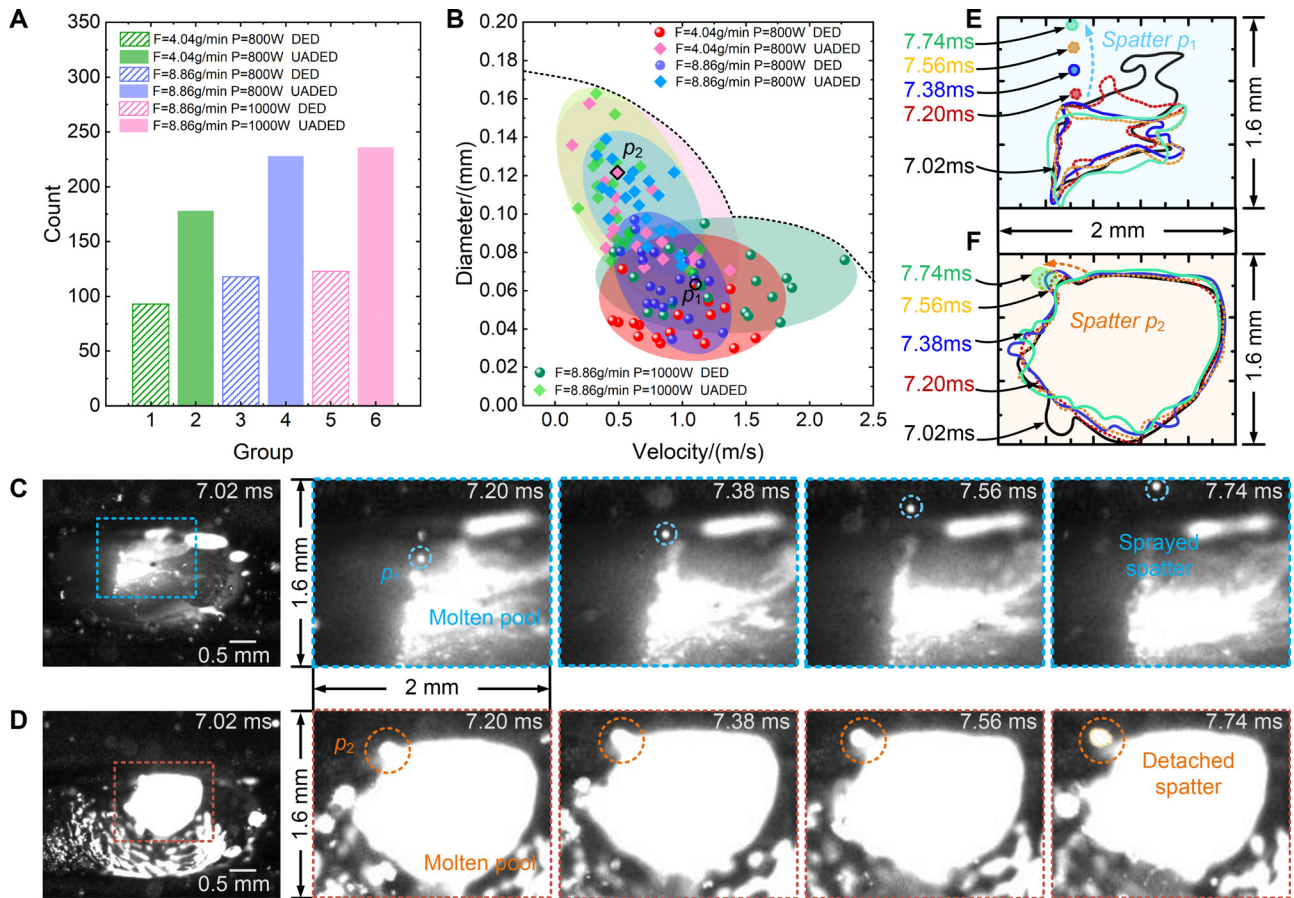


**FIG. 3.** Spatter formation, motion, and quantitative behavior in DED and UADED. (a) Spatter population statistics in DED and UADED within 0–470 ms. Due to the spatial resolution of the optical photographs, here, only the spatters with the sizes of  $20\text{--}180 \mu\text{m}$  are tracked to ensure statistical reliability. (b) The correlation between spatter initial velocity and size (equivalent diameter) during DED with and without ultrasound, in which the scanning speed is constant at 360 mm/min. Twenty spatters for each parameter set are randomly selected. (c) and (d) Representative optical images of formation and motion of spatter  $p_1$  (sprayed) and spatter  $p_2$  (detached) marked in (d) during DED and UADED, respectively. The zoom-in snapshots (7.20–7.74 ms) are from the blue and orange dashed boxes in the optical images of 7.02 ms. (e) and (f) Contours of the sprayed spatter  $p_1$  and detached spatter  $p_2$  under time frame of 7.02, 7.20, 7.38, 7.56, and 7.74 ms, showing as the irregular solid curved lines distinguished by color. Blue and orange dashed arrows indicate the ejection trajectory of the sprayed spatter  $p_1$  and the detached spatter  $p_2$  over time, respectively.

in UADED. Moreover, the laser power significantly influences the track geometries in both DED and UADED; the track width and track depth increase with the laser power, while the powder feed rate has little effect on the track geometries. A slow scanning speed can slightly enlarge the track width and depth in UADED, but does not obviously impact those in the DED process.

### B. Surface defects in UADED

Unfortunately, the ultrasound is found playing a negative role on the surface finish. Bulges and depressions alternately arise, and coarse tilt ripples are distributed ubiquitously on the track surface [Figs. 5(a-A1) and 5(a-A2), Multimedia view]. When continuously depositing materials layer by layer in UADED, more severe defects on the track surface emerge, mainly including discontinuity, large bulges, and depressions, which can cause failure of the deposition process after certain layers [Fig. 4(c)]. We ascribe these surface imperfections to the

instability of the tail zone. The layer height is measured after deposition, while the corresponding tail zone length (TZL) is captured using the high-speed camera. Obviously, the variation of the layer height is similar to the corresponding TZL during UADED [Fig. 5(b)]. The layer grows first until the TZL reaches a threshold. The layer height then decreases gradually with the decreasing TZL, which forms a depressed layer surface. In addition, the width of the tail zone fluctuates as well, thus some coarse tilt ripples remain on the layer surface after molten pool solidifies. According to the simulation and experimental results [Figs. 5(a)–5(f)], the aforementioned flow mode during UADED is responsible for the fluctuation of the TZL. As indicated in the simulation of two-layer UADED, the mushy zone is rather large and the liquid material region becomes very small [Fig. 5(c)]. With the melting front moving forward, the mushy zone becomes larger and the solid fraction increases at the end of the tail zone. When the solid fraction reaches the critical solid fraction, the velocity can be neglected, inducing the decrease in the TZL. In addition, we find

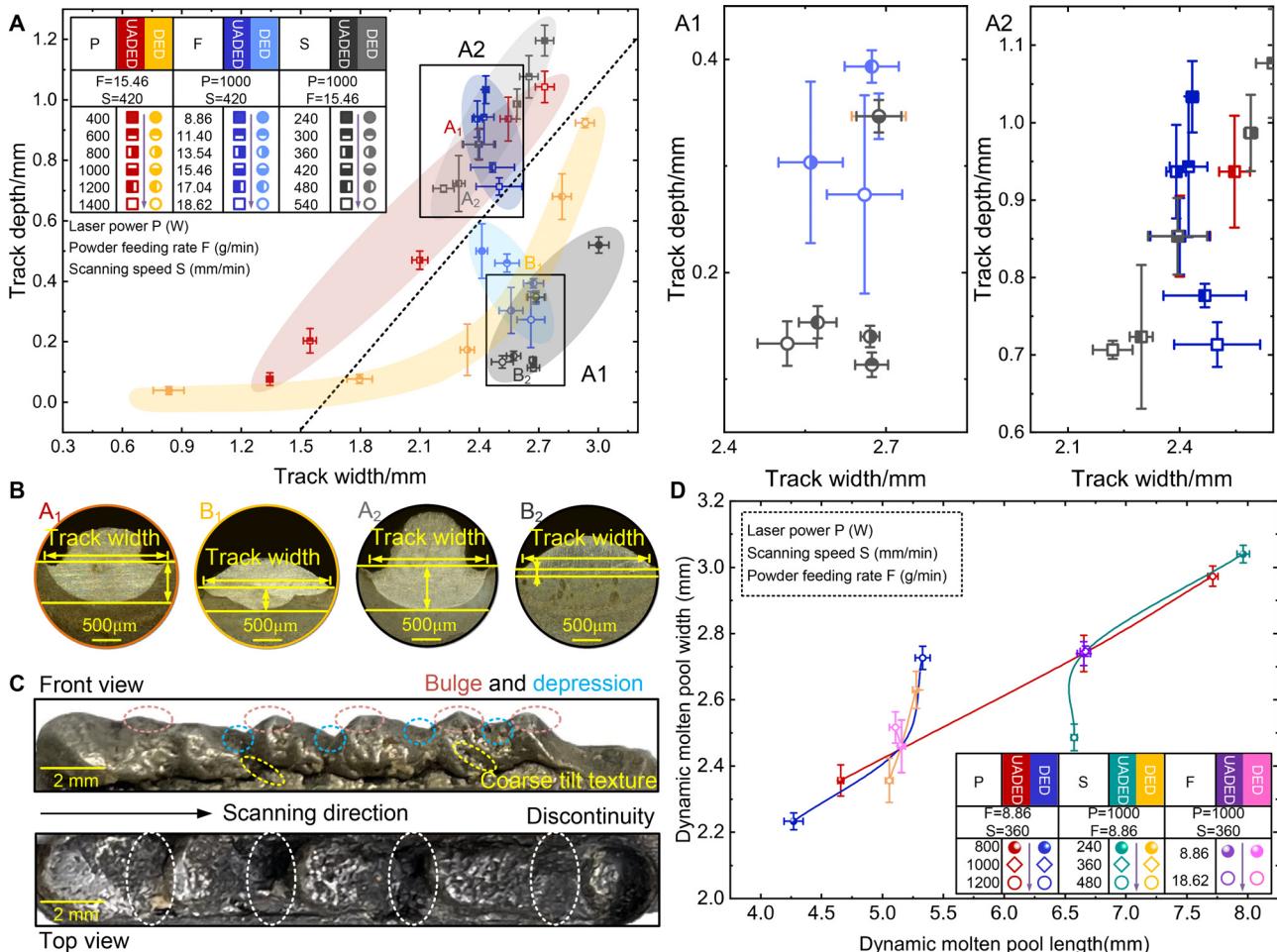


**FIG. 4.** Analysis of the liquid–solid transition characteristics. (a) Size changes in the cross section of the solidified tracks. The inset in (A1) and (A2) shows a zoomed-in plot for the relationship between track width and track depth. (b) Morphologies in the cross section of the solidified tracks, corresponding A<sub>1</sub>, A<sub>2</sub>, B<sub>1</sub>, B<sub>2</sub> marked in (a). (c) Snapshots showing the solidified surface defects in UADED, including the bulge and depression, coarse tilt texture, and the discontinuity. (d) The effects of process parameters on the dynamic size of the molten pool.

that the TZL threshold differs with each other under different parameter sets [Fig. 5(b)]. Basically, the threshold is high when the laser power is high or the scanning speed is slow. Considering the periodic changes of layer height, for each parameter set, we look into a single cycle of layer height variation [see the red rectangle region in Fig. 5(b)]. The slow scanning speed or large laser power can obviously increase the period, resulting in diminishing occurrence of the bulge and depression on solidified surface. Moreover, the relative standard deviations of layer height from case 1 to case 4 are 13.84%, 11.28%, 13.18%, and 12.31%, respectively, which indicates that the fluctuations of layer height for different parameter sets are at a similar level. Overall, the UADED process with high power density (large laser power or slow scanning speed) has potential to reduce the severe surface unevenness, but it can also induce more serious spatter ejection, significantly decreasing the layer surface quality. Therefore, simple parameter optimization cannot effectively improve the layer quality.

To fully eliminate the inevitable surface defects during UADED, a hybrid deposition method where UADED and DED are alternately employed between layers is proposed to avoid this problem; e.g., one layer is processed by UADED with a fast scan speed while the next layer is deposited without ultrasound and a relatively slow speed. This method can mitigate the discontinuity and serious surface variation without sacrificing the building speed. Moreover, the multilayer fabrication process runs in the laser/powder negative defocusing state. Our previous study found that an uneven track surface can be self-regulated in the negative defocusing state.<sup>64</sup> This method helps to eliminate the unevenness on the track surface.

### C. Microstructure and property

The schematic diagrams of DED and UADED are shown in Fig. S7. Besides depression and fish-scale ripples, cavitation is another unique phenomenon during UADED. In this study, we do not capture

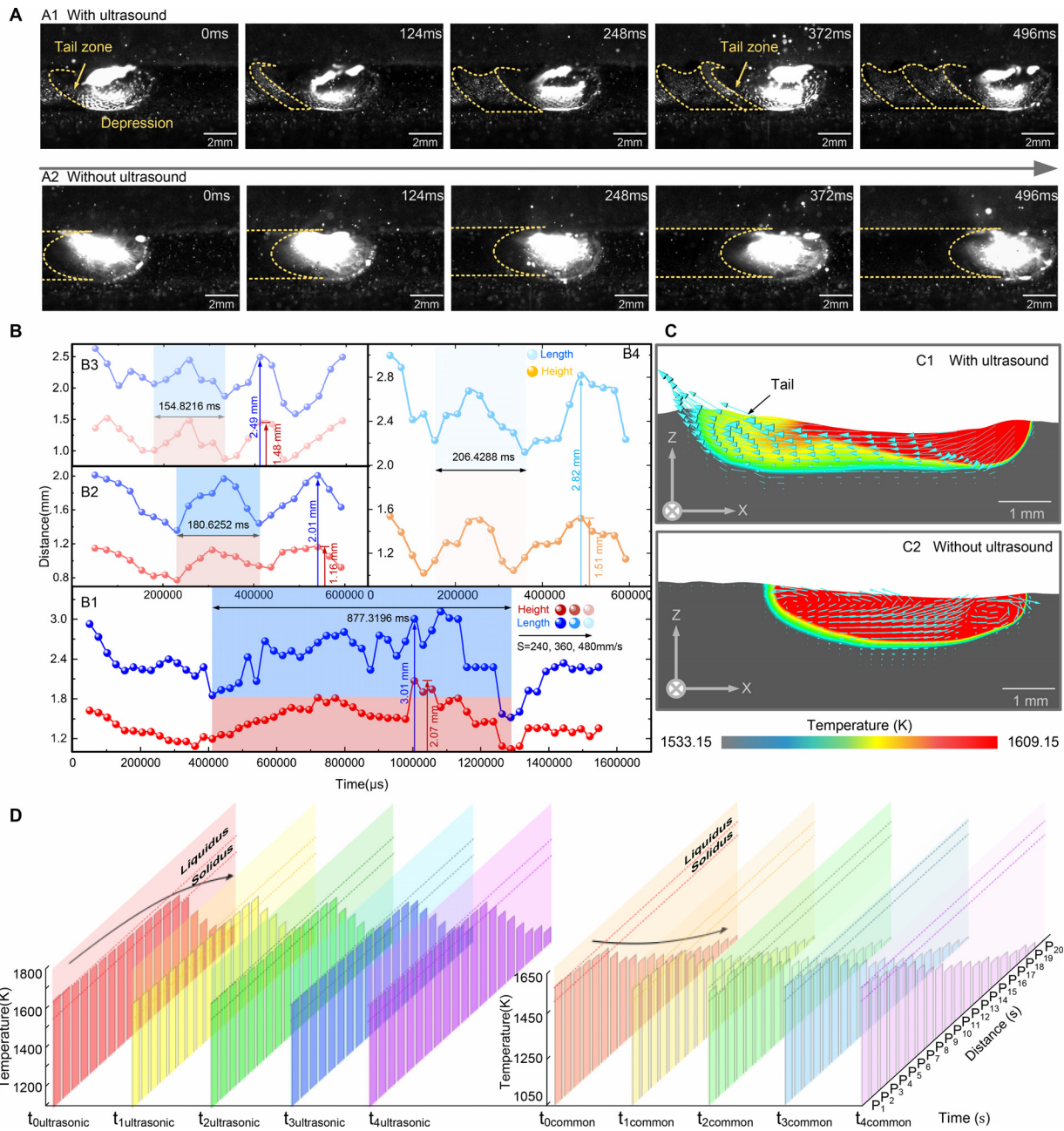


**FIG. 5.** Effects of flow on solidified surface defects. (a) Snapshots showing two-layer DED formation processes with and without ultrasound where the laser power is 1000 W, the powder feed rate is 8.86 g/min, and the scanning speed is 360 mm/min. (b) The changes of the tail zone length and height of molten pool with time during UADED. The experimental parameters are as follows (B1, B2, B3):  $P = 1000$  W,  $F = 8.86$  g/min,  $S = 240, 360, 480$  mm/min; B4:  $P = 1200$  W,  $F = 8.86$  g/min,  $S = 360$  mm/min. (c) The flow field in the two-layer simulation. (d) Twenty locations ( $P_1$ - $P_{20}$ ) were selected at equal distances within 3 mm from the edge of the molten pool, and statistical analysis was on temperature changes at five moments during UADED ( $t_{\text{ultrasonic}}-t_4$ ) and DED ( $t_{\text{common}}-t_4$ ). The time interval is 5 ms. Multimedia views: <https://doi.org/10.1063/5.0082461.9>; <https://doi.org/10.1063/5.0082461.10>

clear images of the cavitation bubbles; instead, calculations are used to judge whether the cavitation has occurred.<sup>18</sup> The calculated ultrasonic intensity is over  $2 \times 10^7$  W·m<sup>-2</sup> for molten Ni, which is much larger than the cavitation threshold ( $\sim 10^6$  W m<sup>-2</sup>) in Ref. 32. That is, the

employed ultrasound has great potential to produce cavitation bubbles in the molten pool. The cavitation bubbles initially form in the rarefaction phase, grow gradually after several cycles of rarefaction and compression phases and finally collapse in the compression phase

[Fig. S7(e)].<sup>65</sup> During this process, the bubbles move around the molten pool, carry away the latent heat of vaporization and stir the surrounding fluid, which enhances the localized convection in the molten pool.<sup>66</sup> When the cavitation bubbles collapse and burst, a large amount of heat will be emitted. Moreover, the depression on the molten pool surface can induce more laser reflections and enhance the laser absorptivity. Therefore, the relevant severe phenomena (e.g., cavitation, fluid flow) during UADED part possess potential to induce preferable microstructures during the hybrid deposition.

With the aforementioned hybrid processing method, a layered microstructure can be produced in which coarse and fine grains

alternately appear [Figs. 6(a)–6(c)]. As expected, both the left- and right- zone displayed in Figs. 6(d)–6(f) corresponding to DED process primarily consist of coarse columnar grains growing along the deposition direction. However, the middle-zone deposited by UADED is dominated by equiaxed crystals. These equiaxed primary  $\gamma$  grains appear as random crystallographic textures compared to the counterpart by DED [Figs. 6(g) and 6(h)]. Further statistical results show the average size of the grains within the DED region is  $98.51 \mu\text{m}$ , and distinctly finer grains with the average size of  $13.91 \mu\text{m}$  appear in the UADED region, demonstrating that UADED refines the grains significantly. The columnar to equiaxed transition (CET) in the region with

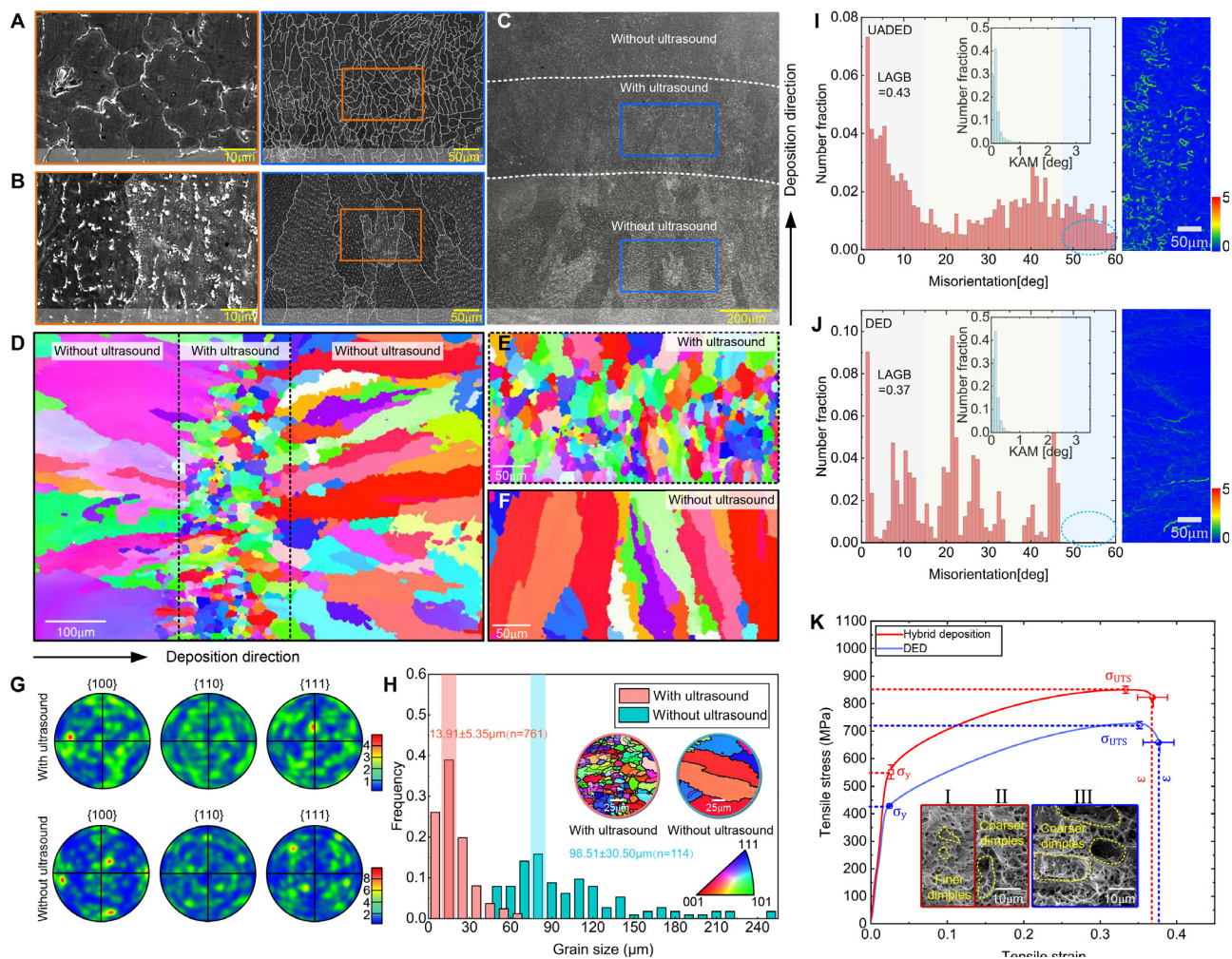


**FIG. 6.** Microstructure and tensile properties by hybrid deposition and comparisons with the counterparts by DED. (a) and (b) are the local microstructures with different magnifications which represent the fine-grain layer (with ultrasound) and coarse-grain layer (without ultrasound), and both of them are extracted from one sample (c) showing hybrid structure. (d) The inverse pole figure maps along the build direction (z) for the  $\gamma$  phase in samples produced by the hybrid deposition strategy, and (e) and (f) the deposited layer with- and without- ultrasound, respectively. (g) the (100), (110), (111) contoured pole figures (in MUD: multiples of uniform distribution) of  $\gamma$  phase which are obtained along the build direction, and the first row and second row correspond to samples with and without ultrasound. (h) The statistics of the grain size of as-built Inconel 718 part, red for UADED while blue for DED. (i) The grain boundary map and KAM map of the fine-grained layer produced in hybrid deposition [comparisons with the coarse grain layer (j)]. (k) tensile properties of Inconel 718 part fabricated by hybrid deposition and DED, respectively. The error bars stand for standard deviation. The respective fracture surfaces of hybrid deposition (I) and (II) and DED (III) are inserted in (h), where I and II compose the hybrid deposition internal microstructure and they correspond to the UADED layer and DED layer.

ultrasound may be related to process parameters, fluid flow in the mushy zone and ultrasound induced cavitation. For the first probability, an extended Hunt criterion<sup>67</sup> is used to evaluate whether the CET can happen in the region with ultrasound based on the temperature gradient and dendrite growth rate near the solidus temperature regime obtained from simulation. The detailed description for this method is illustrated in the [supplementary material](#). The results show that the value of  $G^2/V$  is larger than the threshold beyond which fully columnar forms. This indicates that with the current parameter set, CET cannot happen in the region with ultrasound. The flow stress in the mushy zone is also calculated ([supplementary material](#)). The maximum flow stress (22 MPa) in a cycle of melt periodic flow is close to the calculated yield strength of Inconel 718 at melting point (37.3 MPa).<sup>68,69</sup> Furthermore, the high frequency oscillation of melt can initiate cracks on the root of dendrite arms and introduce high temperature liquid into the mushy zone, promoting the fatigue fragmentation of dendrite arms.<sup>70,71</sup> The fragmentation not only reduces the size of dendrite, but also prompts the generation of numerous nuclei or crystallites. Therefore, the fluid flow in the mushy zone has the potential to induce equiaxed grains. The applied ultrasound intensity far exceeds the threshold of cavitation in molten Inconel 718 in the study. A large number of cavities are expected to occur and further activate the nuclei in the alloy. The formation of new grains leads to an enlarged zone of equiaxed grains. In general, the CET in the region with ultrasound results from the large-velocity high-frequency fluid flow in the mushy zone and ultrasound induced cavitation.

More profoundly, such layered microstructure shows great potential for improving tensile strength.<sup>72</sup> In hybrid deposition, the yield strength  $\sigma_y$  (improved by 28%) and ultimate tensile strength  $\sigma_{UTS}$  (improved by 15%) are higher than that of DED because of the presence of fine-grained layer [Figs. 6(k) and S11(c) and Table S4]. The higher yield strength in hybrid deposition with finer grains [Figs. 6(a)–6(f)] can be rationalized by the Hall-Petch ( $\sigma_y = \sigma_0 + kd^{-1/2}$ ,  $\sigma_0$ : friction stress;  $k$ : material constant;  $d$ : grain size).<sup>18</sup> In addition, we find a slight decrease in plasticity of the counterparts by UADED. It can be elucidated from the perspective of fracture morphology. Mixed fracture (i.e., quasi-cleavage fracture and ductile fracture with dimples) occurs in the hybrid deposition samples, and the dimples are relatively small, which is dissimilar with the main fracture features of the larger dimples in DED parts [Fig. S11(b)]. In terms of high angle grain boundaries (HAGBs), its frequency in the fine-grained layers with ultrasound [Fig. 6(i)] is obviously lower than that in coarse-grained layers by DED [Fig. 6(j)]. Since the HAGBs can reduce the dislocation density, the presented dislocation density in UADED is relatively high, which also can be proven by the calculated kernel-average-misorientation (KAM) value [Figs. 6(i) and 6(j)].<sup>73</sup> On the other hand, more low angle grain boundaries (LAGBs) in the fine-grained layer make crystal slipping harder to occur.<sup>74,75</sup>

#### IV. CONCLUSION

In summary, we leveraged *in situ* high-speed imaging and high-fidelity multi-physics modeling to uncover the flow characteristics of molten pool during UADED, that is periodic forward and backward flow along the vibration direction under the effect of ultrasound induced inertial force. This unique flow mode gives rise to a depression molten pool with fish-scale ripples as well as severe surface defects after solidification. A hybrid deposition method where UADED and

DED are alternately employed between layers is developed to mitigate the surface defects, producing alternating coarse- and fine- grains. Finally, the as-built part obtains 28% and 15% improvement in the yield strength and ultimate tensile strength compared to the counterpart by AM without ultrasound due to this superior layered microstructure.

#### SUPPLEMENTARY MATERIAL

See the [supplementary material](#) for supporting notes. The molten pool dynamics during low frequency UADED are analyzed. Then, the detailed description for the judgment of parameter induced CET is illustrated. The results show that the value of  $G^2/V$  is larger than the threshold beyond which fully columnar forms. This indicates that with the current parameter set, CET cannot happen in the region with ultrasound. The flow stress in the mushy zone is calculated. The results show that the fluid stress has great potential to initiate cracks on the root of dendrite arms under the high frequency oscillation. The normal DED modeling is also described in the supporting notes. See the [supplementary material](#) Figs. S1–S11, Tables S1–S4, and Video S1.

#### ACKNOWLEDGMENTS

This work was supported by the National Natural Science Foundation of China (No. 51975112) and the Fundamental Research Funds for Central Universities (No. N2003033) and the Liao Ning Revitalization Talents Program (No. XLYC1807063). This research is supported by A\*STAR under its AME IRG Grant (Project No. A20E5c0091).

#### AUTHOR DECLARATIONS

##### Conflict of Interest

The authors have no conflicts to disclose.

##### Author Contributions

Z.C.Y. and S.H.W. conceived the idea. Z.C.Y., S.H.W., and L.D.Z. fabricated the samples. S.H.W. and W.T.Y. performed the simulation. Z.C.Y., S.H.W., and B.X. carried on the experiments. Z.C.Y. and S.H.W. drafted the manuscript, and Z.C.Y., S.H.W., J.S.N., and Y.C.D. interpreted, discussed and edited the manuscript. W.T.Y. and L.D.Z. supervised the work. Z.C.Y. and S.H.W. contributed equally to this work.

#### DATA AVAILABILITY

The data that support the findings of this study are available from the corresponding authors upon reasonable request.

#### REFERENCES

- <sup>1</sup>Z. E. Tan, J. H. L. Pang, J. Kaminski, and H. Pepin, *Addit. Manuf.* **25**, 286 (2019).
- <sup>2</sup>H. Attar, S. Ehtemam-Haghghi, D. Kent, and M. S. Dargusch, *Int. J. Mach. Tools Manuf.* **133**, 85 (2018).
- <sup>3</sup>I. Mathoho, E. T. Akinlabi, N. Arthur, and M. Tlotleng, *CIRP J. Manuf. Sci. Technol.* **31**, 450 (2020).
- <sup>4</sup>Z. G. Zhu, Q. B. Nguyen, F. L. Ng, X. H. An, X. Z. Liao, P. K. Liaw, S. M. L. Nai, and J. Wei, *Scr. Mater.* **154**, 20 (2018).
- <sup>5</sup>H. Wang, Z. G. Zhu, H. Chen, A. G. Wang, J. Q. Liu, H. W. Liu, R. K. Zheng, S. M. L. Nai, S. Primig, S. S. Babu, S. P. Ringer, and X. Z. Liao, *Acta Mater.* **196**, 609 (2020).

- <sup>6</sup>N. A. Kistler, D. J. Corbin, A. R. Nassar, E. W. Reutzel, and A. M. Beese, *J. Mater. Process. Technol.* **264**, 172 (2019).
- <sup>7</sup>S. Sui, H. Tan, J. Chen, C. Zhong, Z. Li, W. Fan, A. Gasser, and W. Huang, *Acta Mater.* **164**, 413 (2019).
- <sup>8</sup>M. Bambach, I. Sizova, J. Sznydler, J. Bennett, G. Hyatt, J. Cao, T. Papke, and M. Merklein, *J. Mater. Process. Technol.* **288**, 116840 (2021).
- <sup>9</sup>L. Yuan, C. O'Sullivan, and C. M. Gourlay, *Acta Mater.* **60**, 1334 (2012).
- <sup>10</sup>J. H. Martin, B. D. Yabata, J. M. Hundley, J. A. Mayer, T. A. Schaedler, and T. M. Pollock, *Nature* **549**, 365 (2017).
- <sup>11</sup>N. Raghavan, R. Dehoff, S. Pannala, S. Simunovic, M. Kirk, J. Turner, N. Carlson, and S. S. Babu, *Acta Mater.* **112**, 303 (2016).
- <sup>12</sup>R. Shi, S. A. Khairallah, T. T. Roehling, T. W. Heo, J. T. McKeown, and M. J. Matthews, *Acta Mater.* **184**, 284 (2020).
- <sup>13</sup>M. M. Kirk, Y. Lee, D. A. Greeley, A. Okello, M. J. Goin, M. T. Pearce, and R. R. Dehoff, *J. Mater.* **69**, 523 (2017).
- <sup>14</sup>I. Todd, *Nature* **549**, 342 (2017).
- <sup>15</sup>X. P. Li, G. Ji, Z. Chen, A. Addad, Y. Wu, H. W. Wang, J. Vleugels, J. Van Humbeck, and J. P. Kruth, *Acta Mater.* **129**, 183 (2017).
- <sup>16</sup>Q. Tan, J. Zhang, N. Mo, Z. Fan, Y. Yin, M. Bermingham, Y. Liu, H. Huang, and M. X. Zhang, *Addit. Manuf.* **32**, 101034 (2020).
- <sup>17</sup>T. C. Lin, C. Cao, M. Sokoluk, L. Jiang, X. Wang, J. M. Schoenung, E. J. Lavernia, and X. Li, *Nat. Commun.* **10**, 2515 (2019).
- <sup>18</sup>C. J. Todaro, M. A. Easton, D. Qiu, D. Zhang, M. J. Bermingham, E. W. Lui, M. Brandt, D. H. StJohn, and M. Qian, *Nat. Commun.* **11**, 142 (2020).
- <sup>19</sup>F. Ning, Y. Hu, Z. Liu, X. Wang, Y. Li, and W. Cong, *J. Manuf. Sci. Eng.* **140**, 105002 (2018).
- <sup>20</sup>C. J. Todaro, M. A. Easton, D. Qiu, M. Brandt, D. H. StJohn, and M. Qian, *Addit. Manuf.* **37**, 101632 (2021).
- <sup>21</sup>T. Yuan, S. Kou, and Z. Luo, *Acta Mater.* **106**, 144 (2016).
- <sup>22</sup>Y. Cui, C. Xu, and Q. Han, *Adv. Eng. Mater.* **9**, 161 (2007).
- <sup>23</sup>P. Madhukar, N. Selvaraj, R. Gujjala, and C. S. P. Rao, *Ultrason. Sonochem.* **58**, 104665 (2019).
- <sup>24</sup>A. Ramirez, M. Qian, B. Davis, T. Wilks, and D. H. StJohn, *Scr. Mater.* **59**, 19 (2008).
- <sup>25</sup>W. Cong and F. Ning, *Int. J. Mach. Tools Manuf.* **121**, 61 (2017).
- <sup>26</sup>F. Ning, D. Jiang, Z. Liu, H. Wang, and W. Cong, *J. Manuf. Sci. Eng. Trans. ASME* **143**, 051009 (2021).
- <sup>27</sup>H. Wang, Y. Hu, F. Ning, and W. Cong, *J. Mater. Process. Technol.* **276**, 116395 (2020).
- <sup>28</sup>F. Wang, I. Tzanakis, D. Eskin, J. Mi, and T. Connolley, *Ultrason. Sonochem.* **39**, 66 (2017).
- <sup>29</sup>F. Wang, D. Eskin, J. Mi, C. Wang, B. Koe, A. King, C. Reinhard, and T. Connolley, *Acta Mater.* **141**, 142 (2017).
- <sup>30</sup>K. S. Suslick, *MRS Bull.* **20**, 29 (1995).
- <sup>31</sup>D. Feng, H. Tan, and J. S. J. Van Deventer, *J. Mater. Sci.* **39**, 571 (2004).
- <sup>32</sup>G. I. Eskin and D. G. Eskin, *Ultrasonic Treatment of Light Alloy Melts* (CRC Press, Boca Raton, 2014).
- <sup>33</sup>W. J. Sames, F. A. List, S. Pannala, R. R. Dehoff, and S. S. Babu, *Int. Mater. Rev.* **61**, 315 (2016).
- <sup>34</sup>C. Panwisawas, B. Perumal, R. M. Ward, N. Turner, R. P. Turner, J. W. Brooks, and H. C. Basoalto, *Acta Mater.* **126**, 251 (2017).
- <sup>35</sup>E. Chauvet, P. Kontis, E. A. Jägle, B. Gault, D. Raabe, C. Tassin, J. J. Blandin, R. Dendivel, B. Vayre, S. Abed, and G. Martin, *Acta Mater.* **142**, 82 (2018).
- <sup>36</sup>V. S. Golubev, *High-Power Lasers Manuf.* **3888**, 244 (2000).
- <sup>37</sup>N. Kumar, S. Dash, A. K. Tyagi, and B. Raj, *Sci. Technol. Weld. Joining* **12**, 540 (2007).
- <sup>38</sup>Z. J. Tang, W. W. Liu, L. N. Zhu, Z. C. Liu, Z. R. Yan, D. Lin, Z. Zhang, and H. C. Zhang, *J. Mater. Process. Technol.* **290**, 116996 (2021).
- <sup>39</sup>C. L. A. Leung, S. Marussi, R. C. Atwood, M. Towrie, P. J. Withers, and P. D. Lee, *Nat. Commun.* **9**, 1355 (2018).
- <sup>40</sup>L. Aucott, H. Dong, W. Mirihanage, R. Atwood, A. Kidess, S. Gao, S. Wen, J. Marsden, S. Feng, M. Tong, T. Connolley, M. Drakopoulos, C. R. Kleijn, I. M. Richardson, D. J. Browne, R. H. Mathiesen, and H. V. Atkinson, *Nat. Commun.* **9**, 5414 (2018).
- <sup>41</sup>M. Bayat, V. K. Nadimpalli, F. G. Biondani, S. Jafarzadeh, J. Thorborg, N. S. Tiedje, G. Bissacco, D. B. Pedersen, and J. H. Hattel, *Addit. Manuf.* **43**, 102021 (2021).
- <sup>42</sup>C. L. A. Leung, S. Marussi, M. Towrie, R. C. Atwood, P. J. Withers, and P. D. Lee, *Acta Mater.* **166**, 294 (2019).
- <sup>43</sup>P. Zhang, X. Zhou, X. Cheng, H. Sun, H. Ma, and Y. Li, *Addit. Manuf.* **32**, 101026 (2020).
- <sup>44</sup>B. Tang, Y. Tan, Z. Zhang, T. Xu, Z. Sun, and X. Li, *Coatings* **10**, 76 (2020).
- <sup>45</sup>K. N. Amato, S. M. Gaytan, L. E. Murr, E. Martinez, P. W. Shindo, J. Hernandez, S. Collins, and F. Medina, *Acta Mater.* **60**, 2229 (2012).
- <sup>46</sup>Z. Yang, L. Zhu, G. Zhang, C. Ni, and B. Lin, *Int. J. Mach. Tools Manuf.* **156**, 103594 (2020).
- <sup>47</sup>D. A. Lesyk, S. Martinez, B. N. Mordyuk, V. V. Dzhemelinsky, A. Lamikiz, and G. I. Prokopenko, *Surf. Coat. Technol.* **381**, 125136 (2020).
- <sup>48</sup>Y. Zhao, K. Li, M. Gargani, and W. Xiong, *Addit. Manuf.* **36**, 101404 (2020).
- <sup>49</sup>S. Wang, L. Zhu, J. Y. H. Fuh, H. Zhang, and W. Yan, *Opt. Lasers Eng.* **127**, 105950 (2020).
- <sup>50</sup>D. R. Liu, S. Wang, and W. Yan, *Mater. Des.* **194**, 108919 (2020).
- <sup>51</sup>W. Yan, W. Ge, J. Smith, S. Lin, O. L. Kafka, F. Lin, and W. K. Liu, *Acta Mater.* **115**, 403 (2016).
- <sup>52</sup>W. Yan, W. Ge, Y. Qian, S. Lin, B. Zhou, W. K. Liu, F. Lin, and G. J. Wagner, *Acta Mater.* **134**, 324 (2017).
- <sup>53</sup>M. Davanipour, H. Javanmardi, and N. Goodarzi, *Iran. J. Sci. Technol.-Trans. Electr. Eng.* **42**, 357 (2018).
- <sup>54</sup>L. Wang, Y. Zhang, H. Y. Chia, and W. Yan, *npj Comput. Mater.* **8**, 22 (2022).
- <sup>55</sup>L. Wang, Y. Zhang, and W. Yan, *Phys. Rev. Appl.* **14**, 064039 (2020).
- <sup>56</sup>C. Hirt and B. Nichols, *Volume of Fluid (VOF) Method for the Dynamics of Free Boundaries* (Flow Science, Inc., 1988), Vol. 107.
- <sup>57</sup>C. England, *Recommended Values of Thermophysical Properties for Selected Commercial Alloys* (Woodhead Publishing Limited, 2011).
- <sup>58</sup>P. Prabhakar, W. J. Sames, R. Dehoff, and S. S. Babu, *Addit. Manuf.* **7**, 83 (2015).
- <sup>59</sup>S. Blairs, *J. Colloid Interface Sci.* **302**, 312 (2006).
- <sup>60</sup>F. Wirth, S. Arpagaus, and K. Wegener, *Addit. Manuf.* **21**, 369 (2018).
- <sup>61</sup>J. C. Haley, J. M. Schoenung, and E. J. Lavernia, *Addit. Manuf.* **22**, 368 (2018).
- <sup>62</sup>A. F. H. Kaplan and J. Powell, *J. Laser Appl.* **23**, 032005 (2011).
- <sup>63</sup>A. T. Sutton, C. S. Kriewall, M. C. Leu, J. W. Newkirk, and B. Brown, *Addit. Manuf.* **31**, 100904 (2020).
- <sup>64</sup>S. Wang, L. Zhu, Y. Dun, Z. Yang, J. Y. H. Fuh, and W. Yan, *Comput. Mech.* **67**, 1229 (2021).
- <sup>65</sup>T. Leong, M. Ashokkumar, and S. Kentish, *Acoust. Aust.* **39**, 54 (2011).
- <sup>66</sup>H. Y. Kim, Y. G. Kim, and B. H. Kang, *Int. J. Heat Mass Transfer* **47**, 2831 (2004).
- <sup>67</sup>G. L. Knapp, N. Raghavan, A. Plotkowski, and T. DebRoy, *Addit. Manuf.* **25**, 511 (2019).
- <sup>68</sup>J. Pilling and A. Hellawell, *Metall. Mater. Trans. A* **27**, 229 (1996).
- <sup>69</sup>H. J. Frost and M. F. Ashby, *Deformation-Mechanism Maps: The Plasticity and Creep of Metals and Ceramics* (Pergamon Press, Oxford, 1982).
- <sup>70</sup>S. Wang, J. Kang, Z. Guo, T. L. Lee, X. Zhang, Q. Wang, C. Deng, and J. Mi, *Acta Mater.* **165**, 388 (2019).
- <sup>71</sup>S. Wang, Z. P. Guo, X. P. Zhang, A. Zhang, and J. W. Kang, *Ultrason. Sonochem.* **51**, 160 (2019).
- <sup>72</sup>D. Li, G. Fan, X. Huang, D. Juul Jensen, K. Miao, C. Xu, L. Geng, Y. Zhang, and T. Yu, *Acta Mater.* **206**, 116627 (2021).
- <sup>73</sup>G. Zheng, B. Tang, Q. Zhou, X. Mao, and R. Dang, *Metals* **10**, 121 (2020).
- <sup>74</sup>C. Li, W. Dai, H. Zhang, Y. Liu, and Y. Zhang, *Eng. Fract. Mech.* **238**, 107287 (2020).
- <sup>75</sup>B. B. He, B. Hu, H. W. Yen, G. J. Cheng, Z. K. Wang, H. W. Luo, and M. X. Huang, *Science* **357**, 1029 (2017).